VANCE PRESS

Rock Mechanics Letters

www.journal-rml.com

Research Article

The effect of loading contact angle on the tensile behavior of rock disks

Mostafa Asadizadeh[1*], Saeed Khosravi[2], Nasrin Abbasssalimi[3], Nima Babanouri[3], Mohammad Rezaei[4], Aref Alipour[5], Veljko Lapčević[6], Ahmadreza Hedayat[7], Taghi Sherizadeh[8]

[1]*Mine Stability West, WSP Global Inc, Denver, CO, USA*
[2]*Faculty of Engineering and Applied Science, Memorial University of Newfoundland, St. John's, Canada.*
[3]*Department of Mining Engineering, Hamedan University of Technology, Hamedan 65155-579, Iran.*
[4]*Department of Mining Engineering, Faculty of Engineering, University of Kurdistan, Sanandaj, Iran.*
[5]*Department of Mining and Metallurgical Engineering, Urmia University of Technology, Iran.*
[6]*The University of Belgrade, Faculty of Mining and Geology, Serbia.*
[7]*Department of Civil and Environmental Engineering, Colorado School of Mines, Golden, CO, USA*
[8]*Department of Mining and Explosives Engineering, Missouri University of Science and Technology, Rolla, MO 65409, USA.*
[*] Correspondence: Mostafa.asadizadeh@wsp.com

Received: 14 October 2024
Revised: 5 August 2025
Accepted: 21 August 2025
Published date: 25 August 2025
Doi: 10.70425/rml.202503.23

Abstract: Tensile strength is one of the most important characteristics of rock masses that could govern the stability of rock structures. Due to difficulties in its direct measurements, indirect methods such as the Brazilian test have been developed to assess the tensile strength of laboratory-scale rock material. This study considers the effect of loading contact angle on the indirect tensile strength of rock-like disks by adopting experimental and discrete element methods. Several experimental specimens made of synthetic materials were examined under diametrical loading, and consequently, a numerical model using PFC3D was calibrated accordingly. Then, the impacts of the loading contact angle (θ) on the tensile strength, failure pattern, and contact force chain were investigated in detail. The results indicated that as θ increases from 0°, suggested by ASTM, to 90°, the tensile state is dominated at the specimen center, whereas for angles greater than 90°, the dominant stress state changed to compression. Also, while σxx (tensile stress) at the center of the disk did not change for θ below 40°, the σyy (compressive stress) and σzz (out-of-plan normal stress) increased after θ =30°. The analysis of developed cracks suggested that when θ is lower than 30°, the percentage of tensile and shear cracks were constant (80% and 20%, respectively). As the loading contact angle increased, tensile cracks decreased, whereas the other increased. By analyzing the failed specimens, three categories of crack patterns and two categories of contact force chains were identified.

Keywords: Indirect tensile strength, Brazilian test, PFC3D, Crack development, Contact force chain

1. Introduction

Tensile strength is an important rock property with a major significance in the design of structures constructed within rocks, such as slopes, pillars, and tunnels, because it can control these structures' mechanical behavior and failure mechanisms. Due to the inherent difficulties of in conducting direct tensile tests on rocks such as clamping, centering, and eliminating bending moment and torque, the tensile strength of rocks is commonly obtained indirectly [1]. Moreover, rock engineers usually deal with various complicated compressive and tensile stress fields. Therefore, obtaining tensile strength while conducting compression loading can yield better results [2].

Brazilian test has been widely adopted to determine the tensile strength of rocks, as their required samples are prepared quickly, and the test procedure is simple [1]. In addition to the effect of loading contact angle, many researchers have made efforts to account for factors affecting tensile strength in Brazilian tests. For instance, the effect of the intermediate principal stress [3,4], rock heterogeneity [5-7], rock anisotropy [8-15], and the impact of frictional force between the loading platens and disk-shaped specimens on their stress distribution [16-18] have been studied along with the cracking process [19-21].

This test could be carried out in accordance with either of the standard methods proposed by the American Society of Testing and Materials [2] or the International Society for Rock Mechanics [22]. However, the loading platens used in these suggested standards are different and this discrepancy may result in different loading contact angles while tensile strength is calculated using the same formula, if the failure crack initiates at the sample center. It has been observed that the crack does not typically propagate at the disk center, which is because the stress state leading to rupture may not be created there [23-27].

The impact of loading contact angle on the tensile behavior of rocks has been investigated analytically [28-31] and experimentally. Erarslan and Williams [32] conducted fracture toughness and Brazilian tests on tuff, sandstone, and granite with loading platens of $\theta = 0^{\circ}$, 15°, 20°, and 30°, and concluded that loading platens with $\theta = 20^{\circ}$ yield closer estimations of the indirect tensile strength (ITS). Komurlu and Kesimal [33] carried out Brazilian tests on eight different rock types using four loading platens with $\theta = 0^{\circ}$, 15°, 20°, and 30° and concluded that the appropriate loading contact angle for determining ITS depends on the rock material.

In addition to analytical and experimental studies, a few researchers have adopted numerical simulations to gain better insights into the effect of loading contact angle on the tensile behavior of rock in Brazilian tests. Erarslan et al. [34] studied tuff specimens numerically using RFPA^{2D} with loading platens of $\theta = 0^{\circ}$, 15°, 20°, and 30°. They established that when θ ranges from 20° to 30°, failure develops at the disk center and that the platen with $\theta = 30^{\circ}$ provides more accurate tensile strength. Komurlu et al. [27] evaluated numerically 19 different types of rocks and rock-like-materials, considering fracture toughness, four loading platens with $\theta = 0^{\circ}$, 15°, 20°, and 30°, and Finite Element Method (FEM). They concluded that the loading contact angle yielding the most accurate results depends on the rock type. Bahaaddini et al. [35] conducted a numerical investigation using FLAC2D, in which disks with θ ranging between 1° to 30° were simulated. This study showed that at lower values of θ, regions of high compressive stresses form at the contacts with the loading platens, and this stress declines as θ rises. Abdullah et al. [36] examined the effect of the contact area of 0% and 8% on stress distribution using FEM and concluded that a higher contact area leads to higher tensile strength. The tensile stresses are distributed over a narrower region along the disk centerline.

However, the numerical investigations into the effect of loading contact angle were mainly carried out using numerical methods other than the Distinct Element Method (DEM) and in two dimensions. Additionally, these studies did not examine the type and orientation of cracks created and the distribution of force chains [37-39]. Moreover, they were limited to loading contact angles of up to 30°, while evaluating the strength behavior of rock disks under different confinement may assist rock

engineers in assessing the tensile strength of rock structures in various confinement conditions, provide them with an in-depth understanding of failure mechanisms, and crack development in rock masses.

The study presented in this paper thoroughly investigated the effect of loading contact angle on the failure pattern, crack development, and force chain in a Brazilian disk subjected to diametral loading through DEM simulations using Particle Flow Code (PFC^{3D}). Particle Flow Code (PFC) has been successfully used to examine crack initiation and propagation, stress distribution, and failure pattern of rocks in Brazilian test [40-43], and the effect of rock heterogeneity on stress distribution [44]. In the present study, the calibration of numerical models was performed using Brazilian disks made of a rock-like material. Then, the effect of loading contact angle on crack development and stress field evolution was studied in detail.

2. Laboratory program

A total of five Brazilian disks and five cylindrical specimens for the uniaxial compressive test were made in the laboratory using rock-like material to calibrate the numerical model. The mix design of this material was the same as the one proposed by Asadizadeh et al. [45]. It contained 40% plaster, 20% cement (type II), and 40% water. The mixture of cement and plaster is beneficial in terms of casting, flexibility, setting time, cost, and accessibility [46-48]. The prepared mixture was poured into cylindrical molds glued to a steel plate, after which the molds were vibrated using a vibrating table for two minutes. This caused the release of air bubbles trapped in the specimens, resulting in sufficient compaction of the specimens. Next, the samples were cured for 14 days at 25°C. Finally, both ends of the specimens were cut to produce level surfaces. The Brazilian disks had a thickness of 27 mm, and the cylindrical samples had a height of 120 mm, while both groups measured 54 mm in diameter. Brazilian and uniaxial compression tests were conducted in compliance with the methods proposed by the International Society for Rock Mechanics [22] (Fig. 1). The mechanical properties of the rock-like material prepared for this study are presented in Table 1.

Fig.1. Experimental tests: Brazilian test, UCS test.

Table 1. Geotechnical characteristic of the tested material

Parameter	Experimental results	SD
σ_c (MPa)	23.70	0.50
E (GPa)	10.53	0.20
ν	0.17	0.05
σ_t (MPa)	3.43	0.10

3. Numerical simulation Program

In this study, the Discrete Element Method (DEM) was adopted to investigate the effect of loading contact angle on the tensile behavior of rock disks [49]. To do so, a three-dimensional Particle Flow Code (PFC^{3D}) was employed to evaluate the stress state, failure pattern, and contact force chain in the specimens.

3.1 Flat-jointed bonded-particle model

This research adopted the flat-joint bonded-particle model (FJ-BPM) to model the intact rock. In this model, to simulate the intact material, a group of particles bonded together is created. In addition, the micro-properties of both particles and bonds determine how the particle assembly behaves under different loading conditions. Each contact created between two balls simulates the behavior of a finite-sized interface between two notional surfaces, each of which is rigidly connected to a particle. The interface is divided into either bonded or unbounded elements [50,51] (see Fig. 2). A bonded element can sustain the applied load unless it exceeds the tensile or shear strength of the bond, meaning that a bonded contact between two particles can sustain partial damage (see Fig. 2). As the bonds break, micro-cracks form and the stress state is redistributed, resulting in further breakage of the bond. When these cracks initiate, propagate, and coalesce, macroscopic fractures emerge.

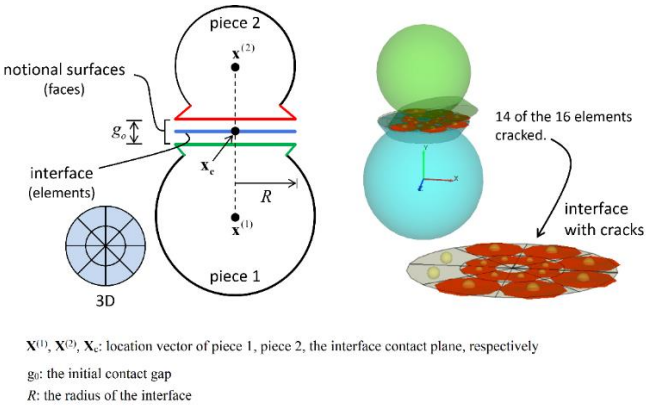

Fig. 2. Flat-joint contact model

3.2 Calibration of Flat-joint BPM

The determination of micro-properties of particles and bonds of a PFC model is carried out through a trial-and-error process, in which the macro-properties recorded in laboratory experiments are obtained [52,53]. This is because there is no direct experimental approach to determine these micro-properties. This process usually involves calibrating the micro-properties against some mechanical parameters of rock obtained from the unconfined compression test and Brazilian test, including uniaxial compressive strength (*UCS*), modulus of elasticity (E), Poisson's ratio (ν), and tensile strength (σ_t) [52,53]. In the first calibration stage, the first three parameters were backcalculated. A PFC model was created to replicate the uniaxial compressive test, which contains a cylindrical specimen with the same dimension as the experimental specimens, and two approaching walls compressing the assembly. The first property that was calibrated was E which depends on the elastic modulus of the particle (E_c), the elastic modulus of the flat-joint bond ($\bar{E}_c$), the particle normal to shear stiffness ratio (k_n/k_s), and the ratio of normal stiffness to shear stiffness of flat-joint bond ($\bar{k}_n/\bar{k}_s$). Then, ν, a function of k_n/k_s, and $\bar{k}_n/\bar{k}_s$, was estimated in an iterative process. In the last step, *UCS*, controlled by the tensile and shear strength of bonds, was calibrated [50-53]. The failure pattern of the numerical model is shown in Fig. 3.

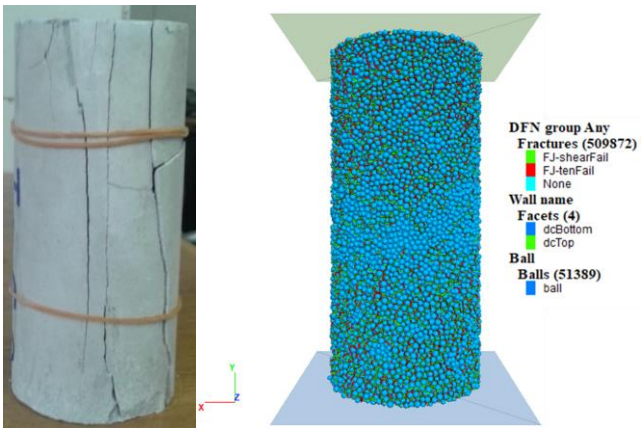

Fig. 3. Failure pattern for a) laboratory and b) numerical samples at rupture for uniaxial compressive tests

The axial stress-axial/lateral strain curves calculated from the results of laboratory tests and numerical simulations are shown in Fig. 4. As can be seen, there is a good agreement between the numerical and experimental results.

The results of the Brazilian test were used to calibrate the tensile strength. The numerical model included two curved walls with the same curvature as the laboratory test moving towards each other and applying diametral load. The dimensions of the Brazilian numerical disks were equal to those of the experimental ones mentioned in section 2. A

measurement sphere was created at the disk center with a diameter of 12.5 mm, and during the simulation process, stress components were recorded over the entire volume of the sphere. The peak value of the stress component in the *x*-direction, i.e., σ_{xx} or tensile stress, was used to evaluate the tensile strength of specimens. The developed fractures at failure are shown in Fig. 5, which shows that the results of numerical simulations agree well with those of laboratory tests.

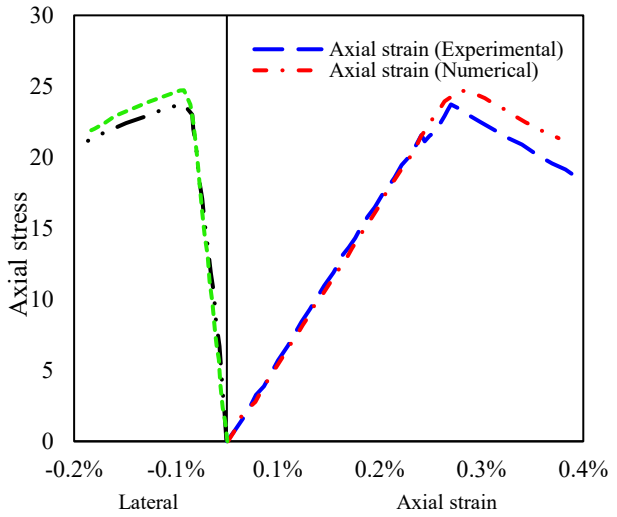

Fig. 4. Stress-strain curve of unconfined compression experiments and calibrated numerical models

Table 2. Calibrated micro-parameters of the flat-joint BPM.

Balls parameters	Value
Density (kg/m^3)	1610
R_{min}(mm)	1.50
R_{max}/R_{min}	1.50
Friction coefficient	0.50
k_n/k_s	3.538
Falt -join BPM parameters	**Value**
$\bar{\lambda}$	1.00
$\bar{E}_c$ (GPa)	10.612
$\sigma_{t\text{-}Fj}$ (MPa)	5.211
c_{Fj} (MPa)	7.075
φ_{Fj}	1.224
$\bar{k}_n/\bar{k}_s$	3.538

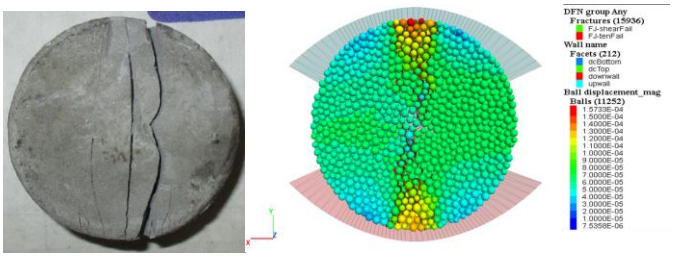

Fig. 5. Comparison between developed cracks in a) experimental and b) numerical models.

The results obtained from the calibration phase are listed in Table 2. In this table, R_{max} and R_{min} are the maximum and minimum ball radii, respectively. k_n/k_s is the normal to-shear stiffness ratio of ball contacts. $\bar{\lambda}$ is the radius multiplier, $\bar{E}_c$ is the elastic modulus of flat joint bonds, $\sigma_{t\text{-}Fj}$, c_{Fj}, and φ_{Fj} are the tensile strength, cohesion, and friction coefficient of flat joint bonds, respectively. $\bar{k}_n/\bar{k}_s$ is the normal to-shear stiffness ratio of a flat joint bond. Results of uniaxial compression and Brazilian tests are presented in Table 3. There are marginal differences between numerical and experimental results.

3.3 Loading platens design

In the numerical models, θ ranged from 0° to 150°. When $\theta \leq 10°$, it changed with an interval of 2°, whereas for higher values of θ, the platens were designed with an interval of 10°. A selected representation of the numerical models is shown in Fig. 6.

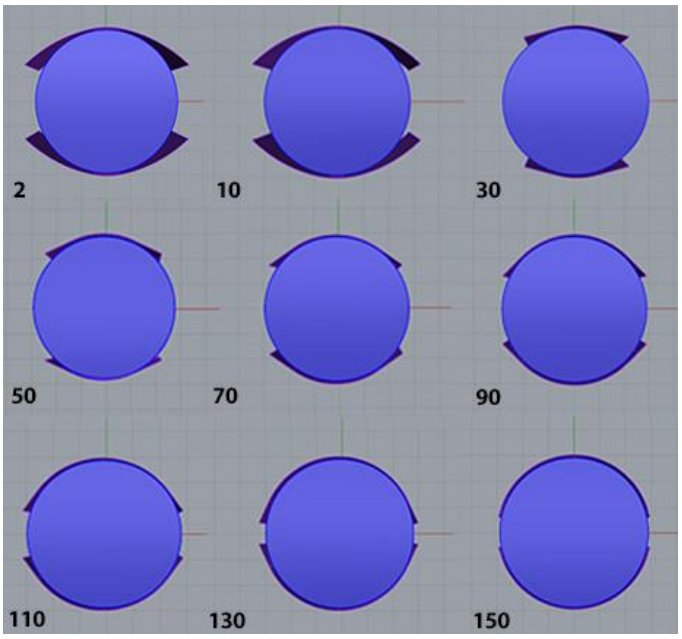

Fig. 6. The variation of contact angle in the Brazilian test

Table 3. Uniaxial tests, physical and calibrated numerical models

Parameter	Experimental	Numerical	Error (%)
E (GPa)	10.53	10.60	0.63
v	0.17	0.17	0.40
σ_c (MPa)	23.70	24.77	4.51
σ_t (MPa)	3.48	3.36	2.09

4. Results and discussion

4.1 Stress state

4.1.1 Normal stresses

Loading contact angle could significantly affect the tensile behavior of a Brazilian disk. In this paper, the negative sign represents compressive stresses, and positive sign represents tensile stresses. The variation of the stress component in the *x*-direction (σ_{xx}) versus θ is shown in Fig. 7. As can be seen, when θ ranged from 0° to 90°, the stress state at the disk center was tensile, whereas, for θ higher than 90°, the stress state turned into compression. In the tensile mode, the maximum tensile stress was obtained when $\theta = 0°$, i.e., the platen was flat, representing the platen proposed by ASTM standard. Moreover, when θ increased from 0° to 40°, there was no significant difference in the maximum of σ_{xx}, which is virtually similar to the results of the numerical investigation reported by Erarslan et al. [32,34] (see Fig. 7). ISRM suggests that θ should be below 15°. Hence, the results for θ between 0° and 15° represent the tensile strength of the specimen tested based on the ISRM suggested method. However, as θ varied from 40° to 90°, σ_{xx} declined considerably, and at θ = 90°, the tensile stress virtually reached zero. This angle is a transition point for the stress state at which tensile stress at the disk center changes to compressive one. For $\theta >$ 90°, σ_{xx} rises, and at θ =100°, it experiences a sudden increase. From θ =100° to θ =130°, σ_{xx} rises considerably, but for $\theta >$ 130°, it increases at a lower rate.

As evident from Fig. 8, the maximum values of the compressive stress, i.e., the stress component in the *y*-direction (σ_{yy}), generally experienced an increasing trend over the entire range of θ. However, when the platen was flat, this stress had its minimum value (well under 25 MPa) and remained nearly unchanged for $\theta \leq 10°$. After that, the stress increased slightly to just over 25 MPa at $\theta = 30°$, followed by a dramatic rise to nearly 65 MPa at θ =100°. Then, as θ increased, σ_{yy} increased at a lower rate, reaching 70 MPa at θ =150°.

On the other hand, the magnitude of the out-of-plane stress, i.e., the stress component in the *z*-direction (σ_{zz}), was remarkably lower than that of σ_{yy}. This stress remained approximately constant when $\theta < 20°$ (see Fig. 9). Its magnitude increased markedly and hit a peak of about -2 MPa at θ = 80° before reaching to roughly -0.25 MPa at θ =150°.

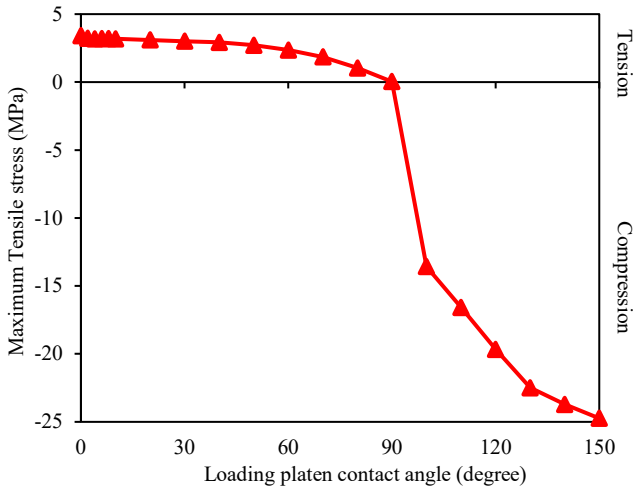

Fig.7. The variation of σ_{xx} at the center of the numerical model versus the loading contact angle

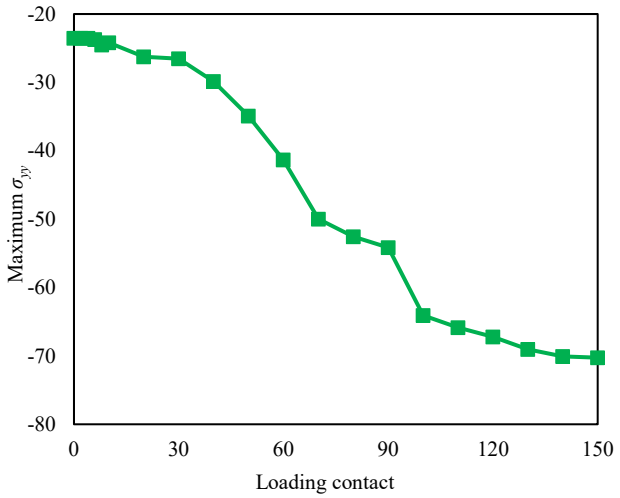

Fig.8. The variation of σ_{yy} at the center of the numerical model versus the loading contact angle

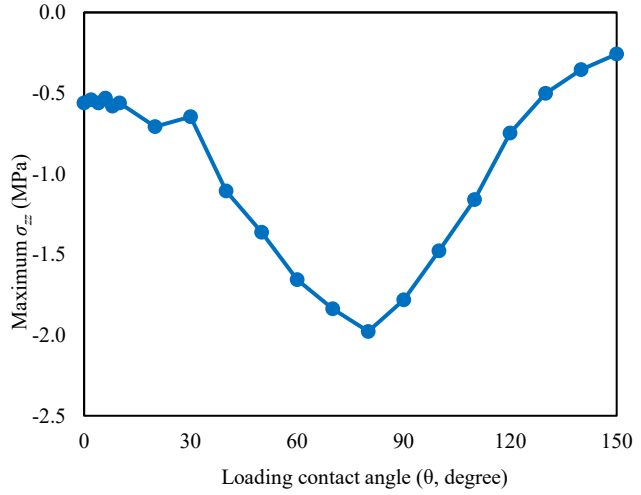

Fig.9. The variation of σ_{zz} at the center of the numerical model versus the loading contact angle

4.1.2 Shear stresses

In regard to shear stresses (see Fig. 10), the main observation was that the magnitude of all the shear stress components was lower than 1 MPa, with the lowest value at $\theta = 0^{\circ}$. The magnitude of σ_{xy} was generally higher than those of σ_{xz} and σ_{yz} except for $\theta = 130^{\circ}$ where it was the lowest.

4.2 Fracture pattern

The fracture pattern of the critical disks is shown in Fig. 13. As evident, when $\theta = 0^{\circ}$, the disk had the narrowest and straightest failure surface compared to all the other specimens (see Fig. 11, $\theta = 0^{\circ}$). Additionally, the resulting cracks evolved along the disk centerline, and more shear cracks formed at its contact with the loading platens. The disk was split into two halves, which could be observed in laboratory experiments [33]. The fracture pattern for $\theta = 2^{\circ}$ differed slightly from that for $\theta = 0^{\circ}$. In comparison, more cracks were generated at the contact of the disk and near the loading platens, and the fractured area was wider than that for $\theta = 0^{\circ}$ (see Fig. 11, $\theta = 2^{\circ}$). The fractures propagated along an oblique line passing through the disk center.

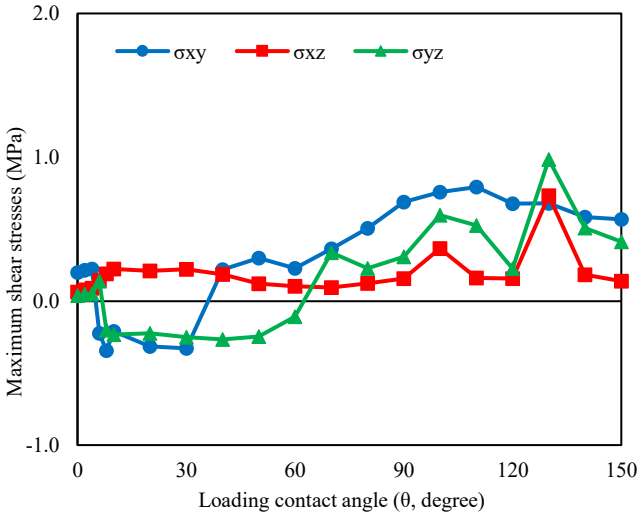

Fig.10. Shear stresses at the center of the numerical model

A different pattern was observed as θ was varied from 4° to 80° (see Fig. 11, θ from 4° to 80°). In these disks, fractures propagate over a larger area of the disk surface, which is limited to two approximately vertical straight lines. In other words, the disks may shatter into a few pieces when they fail, which is consistent with experimental observations [33]. Additionally, this area symmetrically developed around the disk centerline. Furthermore, with an increase in θ, more shear cracks than tensile ones emerged on the disk surface.

Finally, the third pattern appeared for the disks with $\theta \geq 90^{\circ}$ (see Fig. 11, θ from 90° to 150°). As evident, the whole surface of the disks was cracked, and shear cracks dominated the specimens with $\theta \geq 120^{\circ}$.

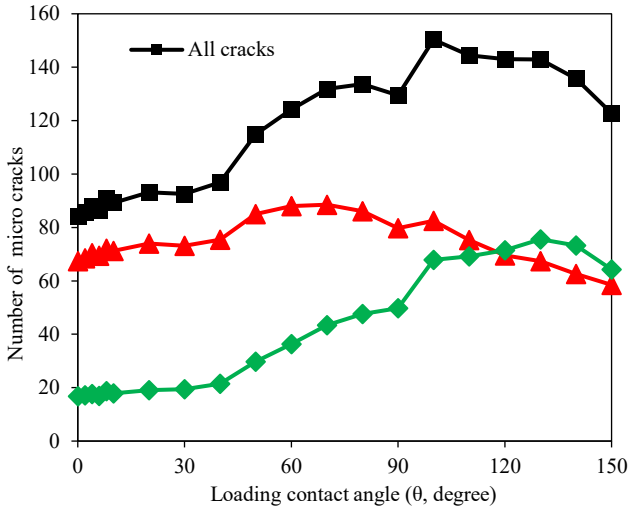

Fig.11. Failure pattern for some of the Brazilian disks

4.3 Crack development analysis

4.3.1 Number of cracks

In this section, the impact of θ on the crack development of Brazilian disks is evaluated. When a Brazilian disk fails, both tensile and shear cracks form. The number of tensile cracks increased steadily from $\theta = 0^{\circ}$ and reached a peak value at $\theta = 60^{\circ}$, after which it experienced a continuous decline (see Fig. 12). In addition, the number of shear cracks increased gradually when θ increased from 0° to 40°, after which this number increased markedly, hitting its maximum value at $\theta = 130^{\circ}$. It then decreased slowly at $\theta = 150^{\circ}$ (see Fig. 12). The total Number of cracks increased steadily to $\theta = 30^{\circ}$, before reaching a peak at $\theta = 100^{\circ}$ (see Fig. 12). Afterward, this number decreased continuously until reaching $\theta = 150^{\circ}$. The trend for tensile cracks differs from that for shear cracks (see Fig. 12).

To better elucidate the variations of the two crack types versus θ, the data on the number of cracks is presented in the form of percentage of the total cracks (see Fig. 13). As it can be seen, when $\theta \leq 30^{\circ}$, the failure of the disk is predominantly caused by tensile cracks, making up to 80 percent of the total cracks. As θ increased, the proportion of tensile cracks declined, and that of shear cracks increased. This means that the contribution of tensile cracks to rupture declined while the contribution of shear cracks to failure increased. Moreover, when $\theta \geq 120^{\circ}$, the proportion of shear cracks exceeded that of tensile ones.

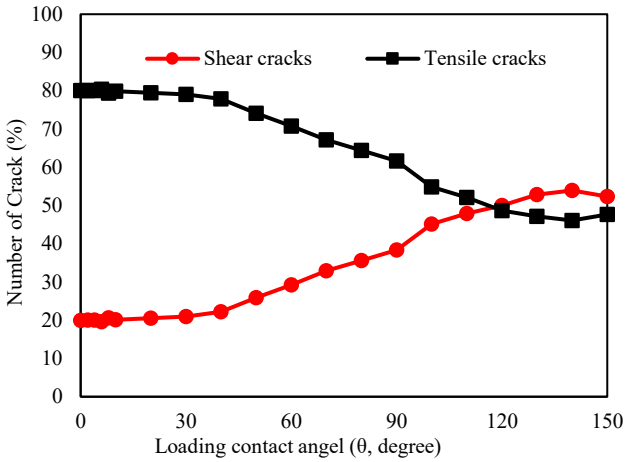

Fig. 12. Cracks number in Brazilian disk versus different curvature angle

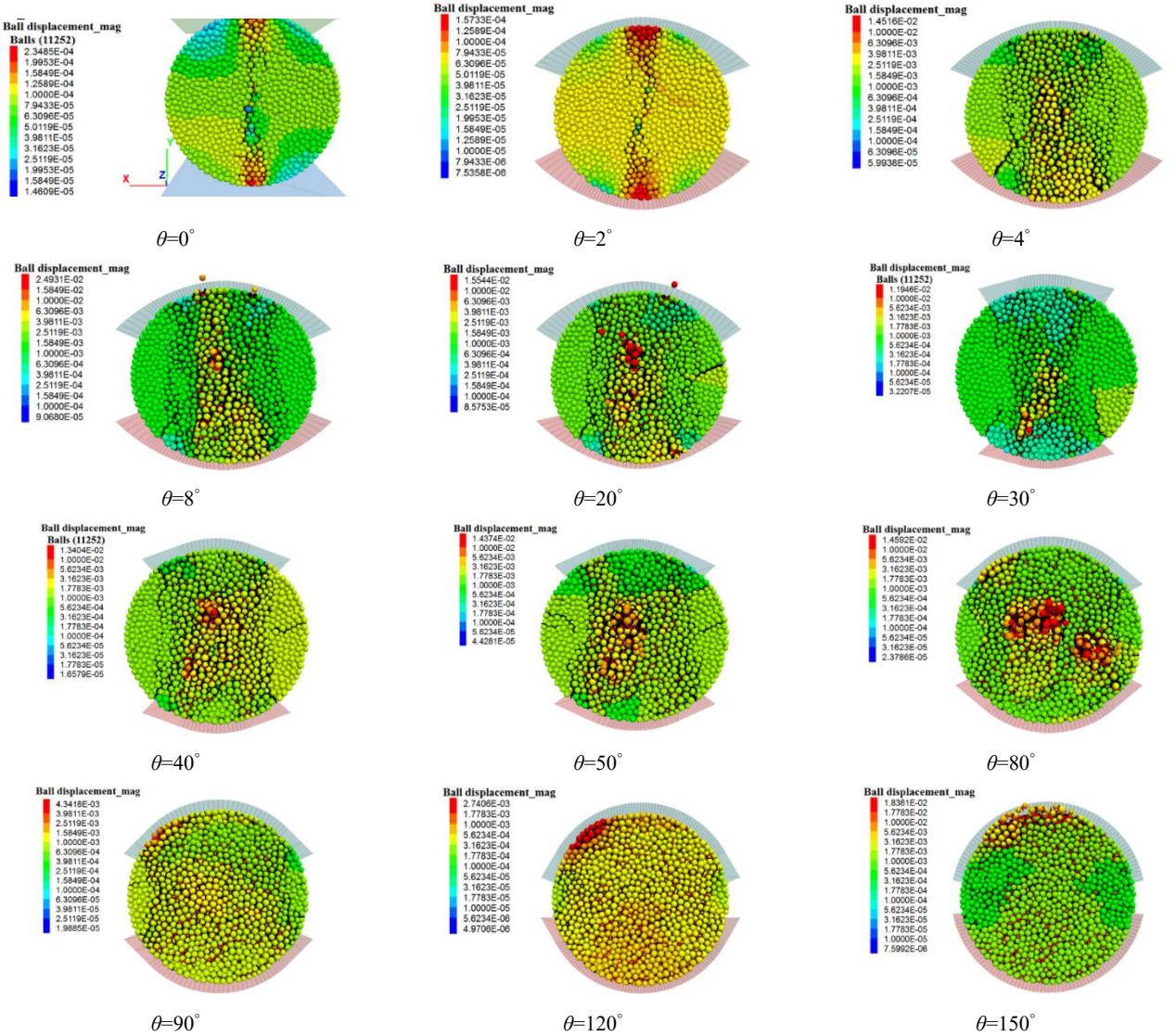

Fig. 13. Variation of the proportion of tensile and shear cracks versus loading contact angle

4.3.2 Crack orientation

As for the orientation of the formed cracks, three distinct categories were identified (see Fig.15). The first one was characterized by one crack set, observable for $\theta = 0^{\circ}$ and 2° (see Fig. 15). When these disks reached the failure, one crack set formed with a dip of 90° and a strike of 0° (see Fig. 14). The second group was observed for $4^{\circ} \leq \theta \leq 40^{\circ}$, in which a conjugate crack system formed. This was reflected in the associated Rosette diagrams, which showed that although cracks with a strike of 0° were still dominant, those with a strike close to 0° and 180° gained dominance too (see Fig. 14, θ from 4° to 40°). A closer look at the corresponding Stereonet diagrams (see Fig. 15, θ from 4° to 40°) reveals that five crack sets were generated in the specimens, one of which was horizontal. Moreover, these diagrams showed that two groups of conjugate cracks, each consisting of two intersecting crack sets, were created in the disks. One of these groups consisted of two vertical conjugate cracks as their pole was located on the perimeter of the Stereonet diagrams. Their strikes were equal to nearly 60° and 105° representing crack sets with strikes of about 150° and 15°, respectively (see Fig. 14 and 15, θ from 4° to

40°). The other two intersecting crack sets had a dip of virtually 45° and a strike of 0° (see Fig. 14 and 15, θ from 4° to 40°).

The third pattern occurred for θ ranging from 50° to 150°. Over this range, cracks tended to grow in all directions. Although for $50^\circ \le \theta < 110^\circ$, the frequency of cracks in a few directions was slightly higher than the others. For $\theta \ge 110^\circ$, cracks propagated equally in every direction (see Fig. 14, θ from 50° to 110°). Moreover, conjugate cracks disappeared, and the dip of the resulting cracks was either horizontal or nearly horizontal. This can be inferred from the associated Stereonet diagrams demonstrating that the concentration of the crack poles increased around the center of the diagrams (see Fig. 15). The Rosette and Stereonet diagrams revealed that as θ increased, the number of cracks with strikes of other than 0° also increased. In addition, the cracks were primarily vertical at lower values of θ, and as θ increased, cracks with lower dips propagated too. In contrast, only horizontal or nearly horizontal cracks evolved at higher values of θ. The evolution of crack strikes can be seen in Fig. 14, in which at the low level of θ, cracks propagated in the direction of diametral load while as θ increased (from θ =110° upward), the joints developed in all directions.

4.3 Contact Force chain pattern

Evaluating the pattern of the contact force chain can help comprehend the failure mechanisms occurring in the Brazilian disks. Both compressive and tensile force chains right before any crack initiation for samples that represent a change in the failure pattern trend are presented in Fig. 16. When the platens were flat, tensile forces were dominant and concentrated vertically along the disk centerline (see Fig. 16, θ = 0°). By contrast, compressive forces were distributed over a larger space and were only significant at the contact of the disk and platen. As the platen became curved and its contact angle increased, tensile forces spread horizontally over a larger space, and compressive ones became more and more dominant throughout the disk (see Fig. 16 from θ = 2° to θ = 90°). For angles above 90°, tensile forces tended to concentrate along the horizontal centerline of the specimen, and as the angle increased, this concentration reduced in a way that for the angle of 150° only small and insignificant concentration of the forces was observable in parts where the platen and disk had no contact. This resulted in the force losing its domination while the compressive forces became dominant.

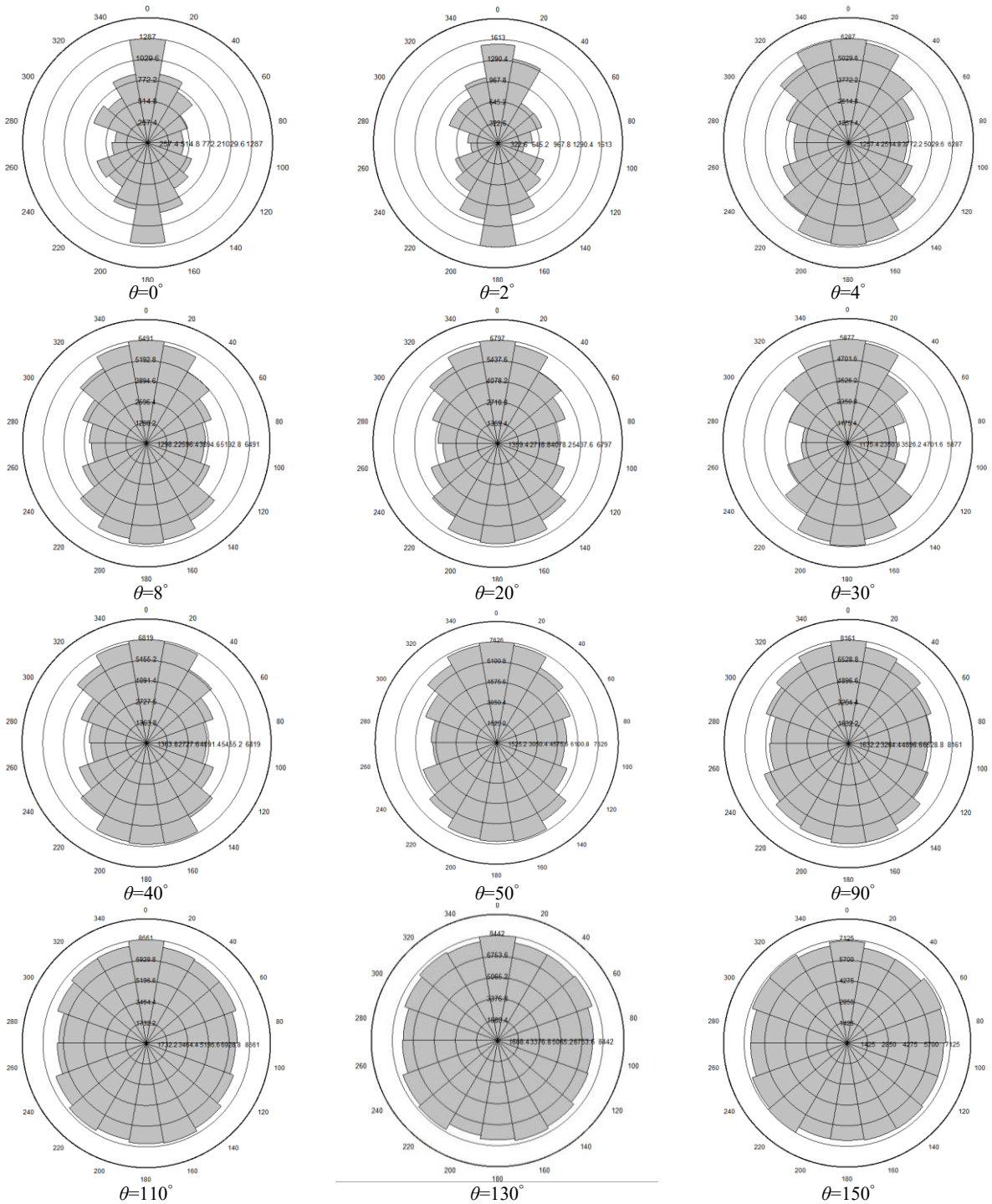

Fig.14. Rosset diagram of all cracks formed in each sample.

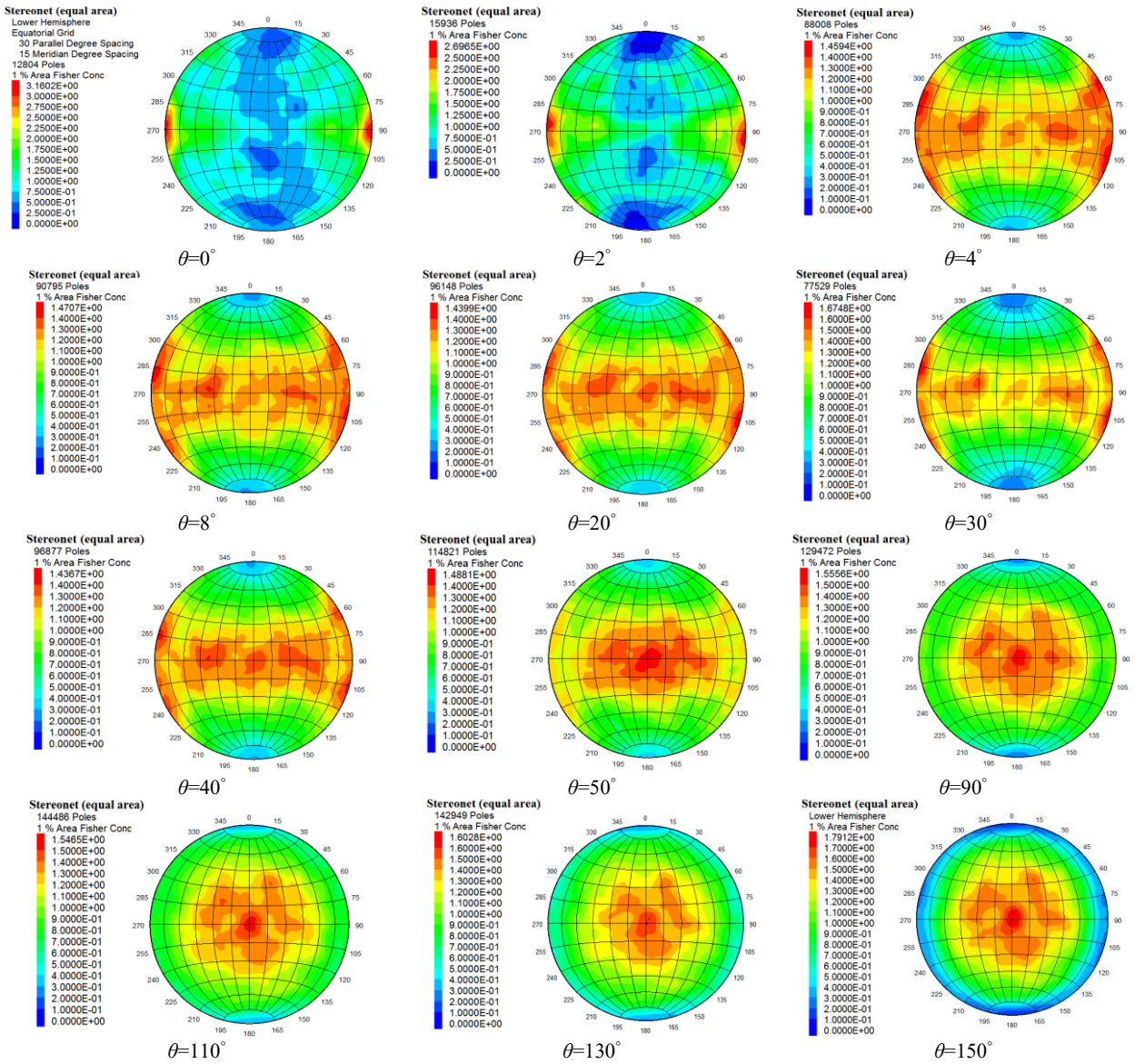

Fig. 15. Stereonet diagram of evolved cracks in samples.

To sum up, the force chain pattern revealed the role of the loading contact angle in whether tensile or compressive forces primarily contributed to fracture initiation in the rock disks. As discussed, tensile force caused the failure of the disk for a lower contact angle, while compressive force played the key role in rupture when the angle was high. When $\theta = 0^{\circ}$ (i.e., ASTM method) tensile force chain concentrated at the center of the disk, while at $\theta = 10^{\circ}$ (i.e., ISRM suggested method), the tensile force chain was wider than the previous one.

5. Conclusion

In this paper, the effects of loading contact angle under a diametral loading condition on the tensile strength, failure pattern, and contact force chain of the Brazilian disk were investigated using PFC^{3D}. The numerical model was calibrated using a uniaxial compressive test and a Brazilian test on rock-like material, and the following key points were made:

At any loading contact angle below 40°, the tensile stress (σ_{xx}) may not change at the center of the disk. The maximum stress was achieved at $\theta = 0^{\circ}$; however, increasing this angle decreased the tensile stress, and after 90°, it turned into compressive stress. Compressive stress (σ_{yy}) at angles below 10° did not change. However, with the increase of θ to 100°, this stress increased, while after this angle, the increasing rate decreased. This means that to reduce the effect of compressive stress on the tensile strength of a Brazilian disk, it is better to reduce the contact angle to lower than $\theta = 10^{\circ}$. At $\theta < 30^{\circ}$, tensile cracks chiefly contributed to the failure process, and their percentage did not change. However, as θ increased, the percentage of tensile cracks declined, and that of shear cracks increased, in addition, when the θ was higher than 120°, the proportion of shear cracks exceeded that of tensile ones.

In general, three fracture patterns were introduced. The first one included disk that had the narrowest and straightest failure surface compared to the other specimens. This happened when $\theta = 0^{\circ}$ and 2°; however, the fractures propagated along an oblique line passing through the disk center for the latter. The second pattern was observed as θ ranged from 4° to 80°. In this group, fractures propagated over a larger disk surface area, limited to two nearly vertical straight lines. The third pattern was identifiable for the disks with $\theta \geq 90^{\circ}$. As evident, the entire surface of the disks was cracked, and shear cracks dominated the specimens with $\theta \geq 120^{\circ}$.In terms of crack formation in the Brazilian disks, three different categories were identified. The first one was characterized by one vertical crack set, which was observable for $\theta = 0^{\circ}$ and 2°. The second group was observed as θ increased from 4° to 40°, forming a conjugate joint system. The last group formed when θ ranged between 50° and 150°, where cracks tended to grow in all directions. The evolution of crack strike showed that at the low level of θ, cracks propagated in the direction of diametral load, while as θ increased (from θ=110° upward), cracks developed in all directions.

As far as the contact force chain is concerned, at $\theta = 0^{\circ}$, tensile forces were dominant and concentrated vertically along the disk centerline. However, compressive forces were distributed over a larger space and were only significant at the contact of the disk and platens. As θ increased, the tensile forces spread horizontally over a larger space, and compressive ones became more dominant throughout the disk. Tensile strength is an important rock property with a major significance in the design of structures constructed within rocks, such as slopes, pillars, and tunnels, because it can control these structures' mechanical behavior and failure mechanisms. Due to the inherent difficulties of in conducting direct tensile

tests on rocks such as clamping, centering, and eliminating bending moment and torque, the tensile strength of rocks is commonly obtained indirectly (Pros et al. 2011). Moreover, rock engineers usually deal with various complicated compressive and tensile stress fields. Therefore, obtaining tensile strength while conducting compression loading can yield better results (ASTM-D3697-16 2016).

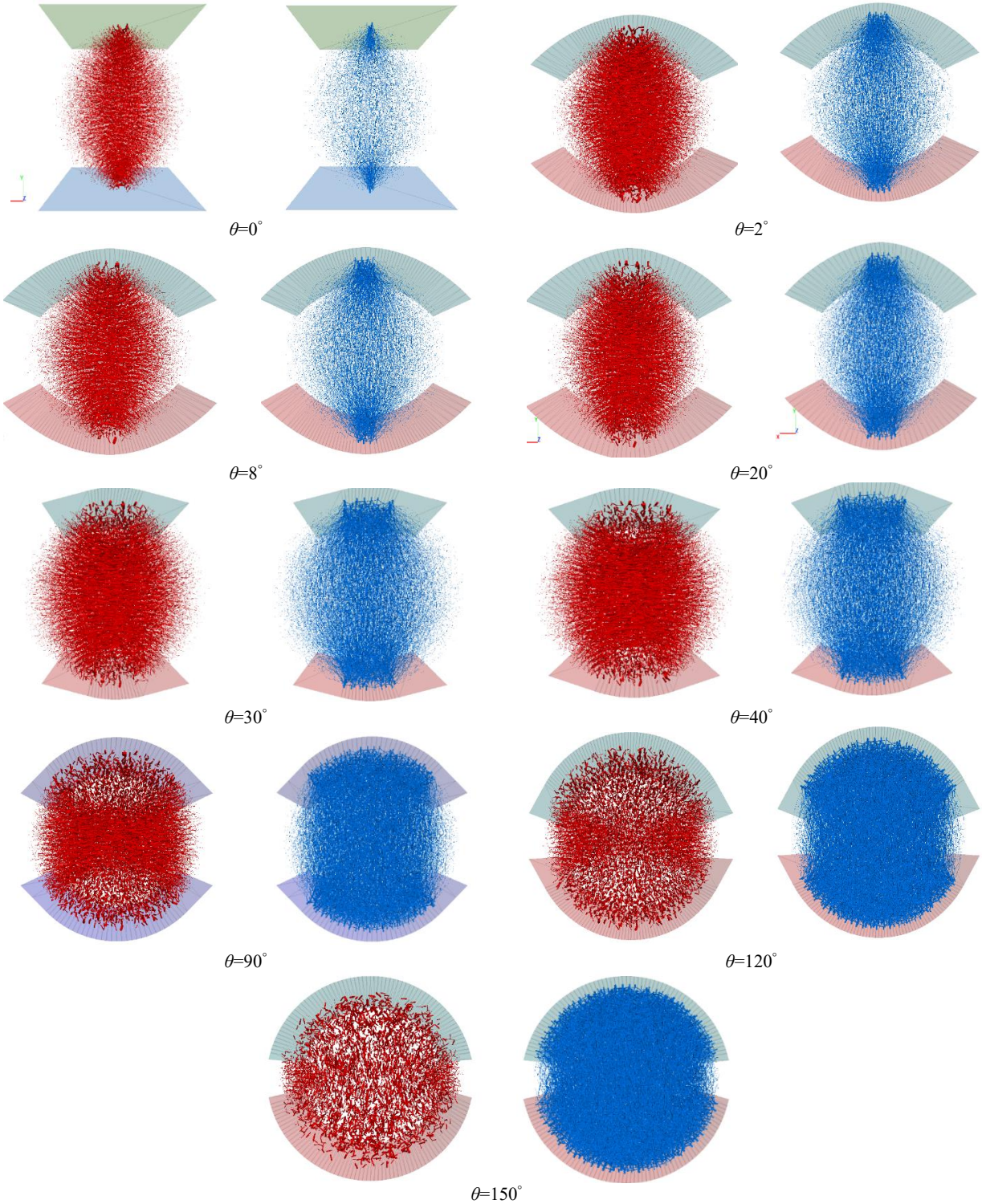

Fig. 16. Contact force chain; Red: tension, Blue: compression

Conflicts of Interest

All the authors claim that the manuscript is completely original. The authors also declare no conflict of interest.

Data availability

All relevant data related to this manuscript are available and can be provided upon reasonable request.

References

1. Pros A, Díez P, Molins C (2011) Numerical modeling of the double punch test for plain concrete. Int J Solids Struct. 48: 1229–1238. https://doi.org/10.1016/j.ijsolstr.2011.01.006
2. ASTM-D3697-16 (2016) Standard test method for splitting tensile strength of intact rock core specimens. In: In Annual book of ASTM standards. West Conshohocken PA: ASTM International. pp 1–3
3. Yu Y, Yin J, Zhong Z (2006) Shape effects in the Brazilian tensile strength test and a 3D FEM correction. Int J Rock Mech Min Sci. 43: 623–627
4. Yu Y, Zhang J, Zhang J (2009) A modified Brazilian disk tension test. Int J Rock Mech Min Sci. 46: 421–425. https://doi.org/10.1016/j.ijrmms.2008.04.008

5. Chen S, Yue ZQ, Tham LG (2004a) Digital image-based numerical modeling method for prediction of inhomogeneous rock failure. Int J Rock Mech Min Sci. 41: 939–957. https://doi.org/10.1016/J.IJRMMS.2004.03.002
6. Chen S, Yue ZQ, Tham LG, Lee PKK (2004b) Modeling Of The Indirect Tensile Test For Inhomogeneous Granite Using A Digital Image-Based Numerical Method. Int J Rock Mech Min Sci. 41: 466–471. https://doi.org/10.1016/J.IJRMMS.2004.03.084
7. Zhu WC, Tang CA (2006) Numerical simulation of Brazilian disk rock failure under static and dynamic loading. Int J Rock Mech Min Sci. 43: 236–252. https://doi.org/10.1016/J.IJRMMS.2005.06.008
8. Tavallali A, Vervoort A (2013) Behaviour of layered sandstone under Brazilian test conditions: Layer orientation and shape effects. J Rock Mech Geotech Eng. 5: 366–377. https://doi.org/10.1016/j.jrmge.2013.01.004
9. Vervoort A, Min K-B, Konietzky H, et al (2014) Failure of transversely isotropic rock under Brazilian test conditions. Int J Rock Mech Min Sci. 70: 343–352. https://doi.org/10.1016/j.ijrmms.2014.04.006
10. Khanlari G, Rafiei B, Abdilor Y (2015) Evaluation of strength anisotropy and failure modes of laminated sandstones. Arab J Geosci. 8: 3089–3102. https://doi.org/10.1007/s12517-014-1411-1
11. Tan X, Konietzky H, Frühwirt T, Dan DQ (2015) Brazilian Tests on Transversely Isotropic Rocks: Laboratory Testing and Numerical Simulations. Rock Mech Rock Eng. 48: 1341–1351. https://doi.org/10.1007/s00603-014-0629-2
12. Mokhtari M, Tutuncu AN (2016) Impact of laminations and natural fractures on rock failure in Brazilian experiments: A case study on Green River and Niobrara formations. J Nat Gas Sci Eng. 36: 79–86. https://doi.org/10.1016/j.jngse.2016.10.015
13. Wang P, Cai M, Ren F (2018) Anisotropy and directionality of tensile behaviours of a jointed rock mass subjected to numerical Brazilian tests. Tunn Undergr Sp Technol. 73: 139–153. https://doi.org/10.1016/j.tust.2017.12.018
14. Feng G, Kang Y, Wang X, et al (2020) Investigation on the Failure Characteristics and Fracture Classification of Shale Under Brazilian Test Conditions. Rock Mech Rock Eng. 53: 3325–3340. https://doi.org/10.1007/s00603-020-02110-6
15. Zhao NN, Feng JL (2021) Investigation on fracture mechanism of layered slate: experiment and beam-particle method. Environ Earth Sci. 80: 788. https://doi.org/10.1007/s12665-021-10106-w
16. Lavrov A, Vervoort A (2002) Theoretical treatment of tangential loading effects on the Brazilian test stress distribution. Int J Rock Mech Min Sci. 39: 275–283. https://doi.org/10.1016/S1365-1609(02)00010-2
17. Dorogoy A, Banks-Sills L (2005) Effect of crack face contact and friction on Brazilian disk specimens—A finite difference solution. Eng Fract Mech. 72: 2758–2773. https://doi.org/10.1016/J.ENGFRACMECH.2005.05.005
18. Markides CF, Pazis DN, Kourkoulis SK (2010) Influence of Friction on the Stress Field of the Brazilian Tensile Test. Rock Mech Rock Eng. 441:113–119. https://doi.org/10.1007/S00603-010-0115-4
19. Serati M, Bahaaddini M, Roshan H, et al (2021) On assessing the tensile cracking pattern in brittle rocks and solids. Bull Eng Geol Environ. 80:.5867–5879. https://doi.org/10.1007/s10064-021-02249-8
20. Serati M, Masoumi H, Williams DJ, Alehossein H (2017) Modified Brazilian Test for Indirect Measurement of Tensile Strength of Brittle Materials. 51st U.S. Rock Mech. Symp. ARMA-2017-0834
21. Wang Z, Yang S, Tang Y (2020) Mechanical behavior of different sedimentary rocks in the Brazilian test. Bull Eng Geol Environ. 79: 5415–5432. https://doi.org/10.1007/s10064-020-01906-8
22. ISRM (2007) The Complete ISRM Suggested Methods for Rock Characterization, Testing and Monitoring; 1974-2006
23. Fairhurst C (1964) On the validity of the "Brazilian" test for brittle materials. Int J Rock Mech Min Sci. 1: 535–546. https://doi.org/10.1016/0148-9062(64)90060-9
24. Lanaro F, Sato T, Stephansson O (2009) Microcrack modelling of Brazilian tensile tests with the boundary element method. Int J Rock Mech Min Sci. 46: 450–461. https://doi.org/10.1016/j.ijrmms.2008.11.007
25. Lin H, Xiong W, Zhong W, Xia C (2014) Location of the Crack Initiation Points in the Brazilian Disc Test. Geotech Geol Eng. 32: 1339–1345. https://doi.org/10.1007/s10706-014-9800-5
26. Wang SY, Sloan SW, Tang CA (2014) Three-Dimensional Numerical Investigations of the Failure Mechanism of a Rock Disc with a Central or Eccentric Hole. Rock Mech Rock Eng. 47: 2117–2137. https://doi.org/10.1007/s00603-013-0512-6
27. Komurlu E, Kesimal A, Demir S (2016) Experimental and numerical study on determination of indirect (splitting) tensile strength of rocks under various load apparatus. Can Geotech J. 53: 360–372. https://doi.org/10.1139/cgj-2014-0356
28. Markides CF, Kourkoulis SK (2012) The stress field in a standardized Brazilian disc: The influence of the loading type acting on the actual contact length. Rock Mech Rock Eng. 45:.145–158. https://doi.org/10.1007/s00603-011-0201-2
29. Markides CF, Kourkoulis SK (2016) The influence of jaw's curvature on the results of the Brazilian disc test. J Rock Mech Geotech Eng. 8: 127–146. https://doi.org/10.1016/j.jrmge.2015.09.008
30. Gutiérrez-Moizant R, Ramírez-Berasategui M, Santos-Cuadros S, García-Fernández C (2018) Computational Verification of the Optimum Boundary Condition of the Brazilian Tensile Test. Rock Mech Rock Eng. 51: 3505–3519. https://doi.org/10.1007/s00603-018-1553-7
31. Gutiérrez-Moizant R, Ramírez-Berasategui M, Santos-Cuadros S, García-Fernández CC (2020) A Novel Analytical Solution for the Brazilian Test with Loading Arcs. Math Probl Eng. 2020: 1–19. https://doi.org/10.1155/2020/2935812
32. Erarslan N, Williams DJ (2012) Experimental, numerical and analytical studies on tensile strength of rocks. Int J Rock Mech Min Sci. 49: 21–30. https://doi.org/10.1016/j.ijrmms.2011.11.007
33. Komurlu E, Kesimal A (2015) Evaluation of Indirect Tensile Strength of Rocks Using Different Types of Jaws. Rock Mech Rock Eng. 48: 1723–1730. https://doi.org/10.1007/s00603-014-0644-3
34. Erarslan N, Liang ZZ, Williams DJ (2012) Experimental and Numerical Studies on Determination of Indirect Tensile Strength of Rocks. Rock Mech Rock Eng. 45: 739–751. https://doi.org/10.1007/s00603-011-0205-y
35. Bahaaddini M, Serati M, Masoumi H, Rahimi E (2019) Numerical assessment of rupture mechanisms in Brazilian test of brittle materials. Int J Solids Struct. 180–181: 1–12. https://doi.org/10.1016/j.ijsolstr.2019.07.004
36. Abdullah R, Tsutsumi T, Amin MFM, et al (2020) Evolution on deformation behaviour of brazilian test under different contact area using particle image velocimetry and finite element modelling. Measurement. 159: 107796. https://doi.org/10.1016/j.measurement.2020.107796
37. Imani M, Nejati HR, Goshtasbi K, Nazerigivi A (2022) Effect of brittleness on the micromechanical damage and failure pattern of rock specimens. Smart Struct Syst. 29: 535–547. https://doi.org/10.12989/SSS.2022.29.4.535
38. Asadizadeh M, Khosravi S, Abharian S, et al (2023a) Tensile behavior of layered rock disks under diametral loading: experimental and numerical investigations. Granul Matter. 25: 21. https://doi.org/10.1007/s10035-023-01311-4
39. Asadizadeh M, Moosavi M, Hossaini MF, et al. (2023b) Numerical Modeling of Rock Blocks with Nonpersistent Rough Joints Subjected to Uniaxial Compressive and Shear Loadings. Int J Geomech. 23: 1–26. https://doi.org/10.1061/ijgnai.gmeng-7858
40. Ma Y, Huang H (2018) DEM analysis of failure mechanisms in the intact Brazilian test. Int J Rock Mech Min Sci. 102: 109–119. https://doi.org/10.1016/j.ijrmms.2017.11.010
41. He J, Afolagboye LO (2018) Influence of layer orientation and interlayer bonding force on the mechanical behavior of shale under Brazilian test conditions. Acta Mech Sin. 34: 349–358. https://doi.org/10.1007/s10409-017-0666-7
42. Yang SQ, Yin P-F, Huang Y-H (2019) Experiment and Discrete Element Modelling on Strength, Deformation and Failure Behaviour of Shale Under Brazilian Compression. Rock Mech Rock Eng. 52: 4339–4359. https://doi.org/10.1007/s00603-019-01847-z
43. Wu S, Ma J, Cheng Y, et al (2018) Numerical analysis of the flattened Brazilian test: Failure process, recommended geometric parameters and loading conditions. Eng Fract Mech. 204: 288–305. https://doi.org/10.1016/j.engfracmech.2018.09.024
44. Sun W, Wu S (2021) A study of crack initiation and source mechanism in the Brazilian test based on moment tensor. Eng Fract Mech. 246: 107622. https://doi.org/10.1016/j.engfracmech.2021.107622
45. Asadizadeh M, Hossaini MF, Moosavi M, et al (2019) Mechanical characterisation of jointed rock-like material with non-persistent rough joints subjected to uniaxial compression. Eng Geol. 260: 105224. https://doi.org/10.1016/j.enggeo.2019.105224
46. Asadizadeh M, Hossaini MF, Moosavi M, Mohammadi S (2016) A laboratory study on mix design to properly resemble a jointed brittle rock. Int J Min Geo-Engineering. 50: 201–210. https://doi.org/10.22059/ijmge.2016.59830
47. Asadizadeh M, Moosavi M, Hossaini MF, Masoumi H (2018) Shear Strength and Cracking Process of Non-persistent Jointed Rocks: An Extensive Experimental Investigation. Rock Mech Rock Eng. 51: 415–428. https://doi.org/10.1007/s00603-017-1328-6
48. Asadizadeh M, Khosravi S, Karimi J, et al. (2022) Mechanical behavior of single-flawed cylindrical specimens subjected to axial loading: a numerical investigation. Bull Eng Geol Environ. 81: 442. https://doi.org/10.1007/s10064-022-02940-4
49. Amir Hosseini M, Kamrava S, Sahimi M, Tahmasebi P (2023) Effect of Wettability on Two-Phase Flow Through Granular Porous Media: Fluid Rupture and Mechanics of the Media. Chem Eng Sci. 269: 118446. https://doi.org/10.1016/J.CES.2023.118446
50. Potyondy DO (2012) A flat-jointed bonded-particle material for hard rock. 46th US Rock Mech Symp 10.
51. Potyondy DO, Cundall PA (2004) A bonded-particle model for rock. Int J Rock Mech Min Sci. 41: 1329–1364. https://doi.org/10.1016/j.ijrmms.2004.09.011
52. Bahaaddini M, Sharrock G, Hebblewhite BK (2013a) Numerical direct shear tests to model the shear behaviour of rock joints. Comput Geotech. 51: 101–115. https://doi.org/10.1016/j.compgeo.2013.02.003
53. Bahaaddini M, Sharrock G, Hebblewhite BK (2013b) Numerical investigation of the effect of joint geometrical parameters on the mechanical properties of a non-persistent jointed rock mass under uniaxial compression. Comput Geotech. 49: 206–225. https://doi.org/10.1016/j.compgeo.2012.10.012